Rigorous broadband investigation of liquid-crystal plasmonic structures using finite-difference time-domain dispersive-anisotropic models

Konstantinos P. Prokopidis,[1] Dimitrios C. Zografopoulos,[2,*] and Emmanouil E. Kriezis[1]

[1]*Department of Electrical and Computer Engineering, Aristotle University of Thessaloniki, Thessaloniki GR-54124, Greece*

[2]*Consiglio Nazionale delle Ricerche, Istituto per la Microelettronica e Microsistemi (CNR-IMM), Roma 00133, Italy*

**Corresponding author: dimitrios.zografopoulos@artov.imm.cnr.it*

Received June 20, 2013; revised August 20, 2013; accepted August 28, 2013; posted August 29, 2013 (Doc. ID 192635); published September 26, 2013

A finite-difference time-domain scheme is proposed for the rigorous study of liquid-crystal photonic and plasmonic structures. The model takes into account the full-tensor liquid-crystal anisotropy as well as the permittivity dispersion of all materials involved. Isotropic materials are modeled via a generalized critical points model, while the dispersion of the liquid-crystal indices is described by Lorentzian terms. The validity of the proposed scheme is verified via a series of examples, ranging from transmission through liquid-crystal waveplates and cholesteric slabs to the plasmonic response of arrays of gold nanostripes with a liquid-crystal overlayer and the dispersive properties of metal–liquid-crystal–metal plasmonic waveguides. Results are directly compared with reference analytical or frequency-domain numerical solutions.

OCIS codes: (050.1755) Computational electromagnetic methods; (160.3710) Liquid crystals; (250.5403) Plasmonics; (240.6680) Surface plasmons; (310.6628) Subwavelength structures, nanostructures.

http://dx.doi.org/10.1364/JOSAB.30.002722

1. INTRODUCTION

Following their widespread use in the field of displays, nematic liquid crystals (LCs), organic materials that share physical properties with both solids and liquids [1], have been under intense investigation as functional materials for the design of novel dynamically tunable photonic components. Their inherent large optical anisotropy, enhanced response to the application of external electric or magnetic fields, and very low driving power requirements have favored their use in numerous photonic devices, ranging from tunable lenses, beam-steerers, and spatial light modulators to guided-wave structures, such as waveguide filters, planar photonic crystals, and microstructured fibers [2,3].

Recently, their use has been expanded in the rapidly advancing field of nanoplasmonics [4] as an efficient means to tune the localized response of metallic nanostructures, such as nanodots [5], nanoholes [6,7], nanodisk arrays [8], and nanoparticle composites [9], targeting the design of electro-optically tunable elements, such as plasmonic switches [10,11]. Furthermore, LC-tunable plasmonic waveguiding components have also been proposed, such as, for instance, attenuators and directional coupler switches for integrated plasmonic circuit architectures [12–16].

When it comes to the design and optimization of advanced LC-photonic structures, theoretical models capable of rigorously taking into account the relevant physics, such as the LC optical properties, are indispensable, owing to the lack of analytical solutions. Various numerical methods have been developed to this end, among which are frequency-domain mode solvers [17], or beam propagation methods [18,19], the latter being very suitable in addressing light propagation in large-scale longitudinal structures. In the case of nanoplasmonic structures, which typically have subwavelength features, the finite-difference time-domain (FDTD) method, a traditional numerical tool for the study of electromagnetic wave propagation [20], constitutes a promising alternative, as it offers broadband characterization by simulating short-pulse propagation in a single run. Moreover, complex media that exhibit frequency dispersion, (bi-)anisotropy, nonlinearity, and inhomogeneity can also be easily tackled in the time domain [21].

The efficiency of the FDTD method in the investigation of LC-plasmonic studies relies on its capability of accurately describing the anisotropic nature of nematic materials as well as the permittivity dispersion of noble metals in the visible. Recently, a permittivity dispersion model based on critical points (CPs) in conjunction with a single Drude term, namely the Drude-critical point (DCP) model, has been shown to describe more efficiently the dispersion of metals in the infrared and visible spectra [22] than the traditional Drude or Drude–Lorentz models, and it has been efficiently implemented in the FDTD method [23–26]. In addition, the full LC anisotropy can also be incorporated by proper definition of the permittivity tensor [27,28]. By merging these two approaches, the DCP model has been combined with an anisotropic FDTD formulation and applied in the tunability studies of plasmonic resonances in periodic LC-metallic nanostructures [29]. Thus far, the FDTD schemes proposed for the study of LC-infiltrated photonic or plasmonic structures incorporate material anisotropy, assuming a constant value for the LC indices that corresponds to a fixed wavelength, but neglect

the LC material frequency dispersion. Nevertheless, plasmonic resonances of nanometallic structures usually occur in the visible range, where the LC indices' dispersion is far from negligible and is typically described by means of a three-coefficient Cauchy model [30]. Since the exact value of the LC indices plays an important role in the position of such resonances [4], a rigorous FDTD scheme should also take into account the dispersion of the elements of the anisotropic permittivity tensor.

In the context of FDTD studies, several algorithms for wave propagation in media that exhibit both anisotropy and dispersive tensor elements have been proposed and implemented, indicatively, via recursive convolution (RC) [31], piecewise linear recursive convolution (PLRC) [32], z-transform [33,34], and auxiliary differential equation (ADE) [35] formulations. In these works, the permittivity tensors of the simulated materials, typically magnetized plasma and ferrites, exhibit dispersion types incapable of describing the frequency dependence of LC tensor elements and, hence, they are not suitable for the numerical investigation of LC-based photonic or plasmonic devices.

In this work, a FDTD scheme is introduced that incorporates both anisotropy and frequency dispersion and permits the rigorous analysis of LC-photonic and/or plasmonic structures. The dispersion of isotropic materials is described by a generalized CP model, while that of the LC is modeled via Lorentzian terms, which are sufficient to accurately describe the dispersion of LC indices. Among the available techniques for the modeling of dispersive media, the ADE formalism has been selected, where the electric flux density is explicitly present as an independent variable. Thus, the proposed scheme can be easily combined with dispersive and anisotropic media, as well as with the convolution perfectly matched layer (CPML), which is employed for efficient truncation of the computational domain [36].

The accuracy of the proposed scheme is tested via a series of key examples, namely transmission through a LC waveplate, a cholesteric liquid-crystal (CLC) slab, the plasmonic resonance study of nanostripe arrays with a LC overlayer, and the modal dispersion properties of a metal–LC–metal (MLCM) plasmonic waveguide. Results are juxtaposed with analytical or numerical methods in the frequency domain, such the Berreman matrix [37] or the finite-element method (FEM) [38], clearly demonstrating the accuracy of the proposed FDTD scheme.

2. FDTD ALGORITHM

A. Modeling of Metals

A new dispersive model for metals has been recently proposed that includes a single Drude term and N critical point pairs [22]. It has been proved in several works that the DCP model can more accurately describe the dielectric dispersion of metals in infrared and optical frequencies than the widely used Drude–Lorentz medium [23,24,39]. The relative dielectric permittivity of the DCP model, assuming $e^{j\omega t}$ time dependence, is described by

$$\varepsilon(\omega)=\varepsilon_\infty+\frac{\omega_D^2}{\omega(j\gamma-\omega)}+\sum_{p=1}^{N}A_p\Omega_p\left(\frac{e^{j\phi_p}}{\Omega_p+\omega-j\Gamma_p}+\frac{e^{-j\phi_p}}{\Omega_p-\omega+j\Gamma_p}\right),\quad(1)$$

where ε_∞ is the relative permittivity at infinite frequency, and ω_D and γ are the plasma frequency and damping coefficient, respectively, of the Drude model, whereas A_p is the amplitude, ϕ_p the phase, Ω_p the frequency, and Γ_p the broadening parameter, respectively, of the pth critical point oscillator [39]. It can be observed that both the Drude and the CP contributions can be included in a more general term, which is an explicit function of the variable $j\omega$,

$$\varepsilon(\omega)=\varepsilon_\infty+\sum_{p=1}^{M}\frac{a_{1p}j\omega+a_{0p}}{b_{2p}(j\omega)^2+b_{1p}j\omega+b_{0p}},\quad(2)$$

where $M=N+1$. It is stressed that the proposed model incorporates all the widely used dispersive models, i.e., Debye, Drude, Lorentz, and static conductivity [26]. The coefficients in Eq. (2) are defined for the case of the DCP model as

$$\begin{aligned}a_{0p}&=2\varepsilon_0A_p\Omega_p(\Omega_p\cos\phi_p-\Gamma_p\sin\phi_p),\\a_{1p}&=-2\varepsilon_0A_p\Omega_p\sin\phi_p,\\b_{0p}&=\Omega_p^2+\Gamma_p^2,\\b_{1p}&=2\Gamma_p,\\b_{2p}&=1.\end{aligned}\quad(3)$$

The relationship between the electric flux density $\mathbf{D}$, the electric polarization $\mathbf{P}$, and the electric field intensity $\mathbf{E}$ in the frequency domain is defined by the following equation:

$$\mathbf{D}(\omega)=\varepsilon_0\varepsilon(\omega)\mathbf{E}(\omega)=\varepsilon_0\varepsilon_\infty\mathbf{E}(\omega)+\mathbf{P}(\omega).\quad(4)$$

The polarization field $\mathbf{P}$ for the case of the DCP model can be expressed as

$$\mathbf{P}(\omega)=\varepsilon_0\chi(\omega)\mathbf{E}(\omega)=\sum_{p=1}^{M}\mathbf{P}_p(\omega),\quad(5)$$

where

$$\mathbf{P}_p(\omega)=\frac{a_{1p}j\omega+a_{0p}}{b_{2p}(j\omega)^2+b_{1p}j\omega+b_{0p}}\mathbf{E}(\omega).\quad(6)$$

The following differential equation is derived after transforming Eq. (6) into the time domain:

$$b_{2p}\ddot{\mathbf{P}}_p(t)+b_{1p}\dot{\mathbf{P}}_p(t)+b_{0p}\mathbf{P}_p(t)=a_{1p}\dot{\mathbf{E}}(t)+a_{0p}\mathbf{E}(t),\quad(7)$$

where single and double dots denote first and second derivatives with respect to time, respectively. After direct discretization of the previous differential equation by using central finite differences of second-order accuracy, one obtains

$$\left(b_{2p}\frac{\delta_t^2}{\Delta t^2}+b_{1p}\frac{\mu_t\delta_t}{\Delta t}+b_{0p}\mu_t^2\right)\mathbf{P}_p^n=\left(a_{1p}\frac{\mu_t\delta_t}{\Delta t}+a_{0p}\mu_t^2\right)\mathbf{E}^n,\quad(8)$$

where δ_t and μ_t are the central difference and average operator over Δt, respectively, according to [40]. These operators are defined as

$$\delta_tF^n=F^{n+1/2}-F^{n-1/2},\quad(9)$$

$$\mu_t F^n = \frac{1}{2}(F^{n+1/2} + F^{n-1/2}), \tag{10}$$

and

$$\delta_t^2 F^n \equiv \delta_t(\delta_t F^n) = F^{n+1} - 2F^n + F^{n-1}, \tag{11}$$

$$\mu_t \delta_t F^n \equiv \mu_t(\delta_t F^n) = \frac{1}{2}(F^{n+1} - F^{n-1}), \tag{12}$$

$$\mu_t^2 F^n \equiv \mu_t(\mu_t F^n) = \frac{1}{4}(F^{n+1} + 2F^n + F^{n-1}). \tag{13}$$

The update equation for $\mathbf{P}_p^{n+1}$ is

$$\mathbf{P}_p^{n+1} = C_{1p}\mathbf{P}_p^n + C_{2p}\mathbf{P}_p^{n-1} + C_{3p}\mathbf{E}^{n+1} + C_{4p}\mathbf{E}^n + C_{5p}\mathbf{E}^{n-1}, \tag{14}$$

where the coefficients C_{ip} are given by

$$C_{1p} = \left(\frac{2b_{2,p}}{\Delta t^2} - \frac{b_{0,p}}{2}\right)\Big/ C_p,$$
$$C_{2p} = \left(\frac{b_{1,p}}{2\Delta t} - \frac{b_{2,p}}{\Delta t^2} - \frac{b_{0,p}}{4}\right)\Big/ C_p,$$
$$C_{3p} = \left(\frac{a_{0,p}}{4} + \frac{a_{1,p}}{2\Delta t}\right)\Big/ C_p,$$
$$C_{4p} = \frac{a_{0,p}}{2C_p},$$
$$C_{5p} = \left(\frac{a_{0,p}}{4} - \frac{a_{1,p}}{2\Delta t}\right)\Big/ C_p, \tag{15}$$

and

$$C_p = \frac{b_{2,p}}{\Delta t^2} + \frac{b_{1,p}}{2\Delta t} + \frac{b_{0,p}}{4}. \tag{16}$$

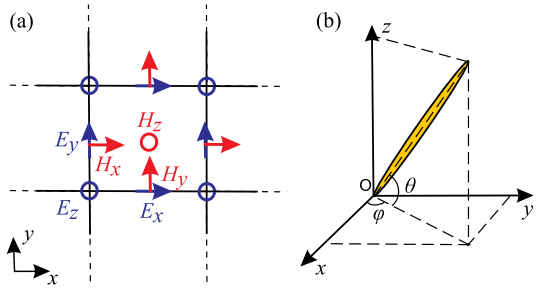

Fig. 1. (a) Definition of the FDTD cell employed in the proposed ADE-FDTD implementation and (b) schematic layout of the nematic molecular director, which is locally described by the tilt (θ) and twist (φ) angles.

The dielectric flux density $\mathbf{D}$ at time step $n+1$ is

$$\mathbf{D}^{n+1} = \varepsilon_0\varepsilon_\infty\mathbf{E}^{n+1} + \mathbf{P}^{n+1}. \tag{17}$$

Substituting $\mathbf{P}^{n+1}$ and solving for $\mathbf{E}^{n+1}$ yields the update equation of the electric field

$$\mathbf{E}^{n+1} = \left(\mathbf{D}^{n+1} - \sum_{p=1}^{N}(C_{1p}\mathbf{P}_p^n + C_{2p}\mathbf{P}_p^{n-1}) - \sum_{p=1}^{N}(C_{4p}\mathbf{E}^n + C_{5p}\mathbf{E}^{n-1})\right)\Big/\left(\varepsilon_0\varepsilon_\infty + \sum_{p=1}^{N}C_{3p}\right). \tag{18}$$

The update of $\mathbf{P}_p$ can then be performed through Eq. (14). The positions of the electric and magnetic field components in the FDTD cell are depicted in Fig. 1(a) for the two-dimensional case. The components of $\mathbf{P}$ and $\mathbf{D}$ are located at the same positions as their respective $\mathbf{E}$ components.

B. Modeling of Liquid Crystals

The relative permittivity tensor of a LC with a random spatial alignment profile can be expressed via the following form [28]:

$$\tilde{\varepsilon} = \begin{pmatrix} \varepsilon_o + \Delta\varepsilon\cos^2\theta\cos^2\phi & \Delta\varepsilon\cos^2\theta\sin\phi\cos\phi & \Delta\varepsilon\sin\theta\cos\theta\cos\phi \\ \Delta\varepsilon\cos^2\theta\sin\phi\cos\phi & \varepsilon_o + \Delta\varepsilon\cos^2\theta\sin^2\phi & \Delta\varepsilon\sin\theta\cos\theta\sin\phi \\ \Delta\varepsilon\sin\theta\cos\theta\cos\phi & \Delta\varepsilon\sin\theta\cos\theta\sin\phi & \varepsilon_o + \Delta\varepsilon\sin^2\theta \end{pmatrix}, \tag{19}$$

where θ and ϕ are the tilt and twist angles, respectively, as shown in Fig. 1(b), ε_o and ε_e are the ordinary and extraordinary dielectric constants, and $\Delta\varepsilon = \varepsilon_e - \varepsilon_o$. In the context of this paper, it is assumed that ε_o and ε_e are functions of frequency and as a result the permittivity tensor exhibits frequency dispersion.

In the following, assuming that the optical axis of the LC is in the x–y plane ($\theta = 0$), the relative permittivity tensor takes the form

$$\varepsilon_{xx}(\omega) = \varepsilon_o(\omega) + \Delta\varepsilon(\omega)\cos^2\phi,$$
$$\varepsilon_{yy}(\omega) = \varepsilon_o(\omega) + \Delta\varepsilon(\omega)\sin^2\phi,$$
$$\varepsilon_{zz}(\omega) = \varepsilon_o(\omega),$$
$$\varepsilon_{xy}(\omega) = \varepsilon_{yx}(\omega) = \Delta\varepsilon(\omega)\sin\phi\cos\phi,$$
$$\varepsilon_{xz}(\omega) = \varepsilon_{zx}(\omega) = 0,$$
$$\varepsilon_{yz}(\omega) = \varepsilon_{yz}(\omega) = 0. \tag{20}$$

The cases of $\phi = 0$ and $\phi = \pi/2$, where the optical axis of the LC lies on the x–z and y–z planes, respectively, lead to similar forms of the permittivity tensor and can be handled according to the methodology presented below. According to the constitutive relation $\mathbf{D}(\omega) = \varepsilon_0\tilde{\varepsilon}(\omega)\mathbf{E}(\omega)$, the components of the dielectric displacement are given by

$$D_x = \varepsilon_0[\varepsilon_o(\omega)\sin^2\phi + \varepsilon_e(\omega)\cos^2\phi]E_x + \varepsilon_0[\varepsilon_e(\omega) - \varepsilon_o(\omega)]\sin\phi\cos\phi E_y, \tag{21}$$

$$D_y = \varepsilon_0[\varepsilon_e(\omega) - \varepsilon_o(\omega)]\sin\phi\cos\phi E_x + \varepsilon_0[\varepsilon_o(\omega)\cos^2\phi + \varepsilon_e(\omega)\sin^2\phi]E_y, \quad (22)$$

$$D_z = \varepsilon_0\varepsilon_o(\omega)E_z. \quad (23)$$

Equations (21) and (22) can be written in the following form in order to split the x and y components of the electric field:

$$P_{x1} = \varepsilon_0\varepsilon_o(\omega)\sin^2\phi E_x, \qquad P_{x2} = \varepsilon_0\varepsilon_e(\omega)\cos^2\phi E_x, \quad (24)$$

$$P_{y1} = \frac{1}{2}\varepsilon_0\varepsilon_e(\omega)\sin(2\phi)E_y, \qquad P_{y2} = -\frac{1}{2}\varepsilon_0\varepsilon_o(\omega)\sin(2\phi)E_y, \quad (25)$$

$$Q_{x1} = \frac{1}{2}\varepsilon_0\varepsilon_e(\omega)\sin(2\phi)E_x, \qquad Q_{x2} = -\frac{1}{2}\varepsilon_0\varepsilon_o(\omega)\sin(2\phi)E_x, \quad (26)$$

$$Q_{y1} = \varepsilon_0\varepsilon_o(\omega)\cos^2\phi E_y, \qquad Q_{y2} = \varepsilon_0\varepsilon_e(\omega)\sin^2\phi E_y. \quad (27)$$

The auxiliary variables P_{x1} and P_{y1} are located at the same positions in the FDTD cell [see Fig. 1(a)] as the related electric fields, E_x and E_y, respectively. The same holds for all the other auxiliary variables above. Keeping expressions (24)–(27) in mind, Eqs. (21) and (22) can be written as

$$D_x = P_{x1} + P_{x2} + P_{y1} + P_{y2}, \quad (28a)$$

$$D_y = Q_{x1} + Q_{x2} + Q_{y1} + Q_{y2}. \quad (28b)$$

A Lorentz model is usually sufficient to describe the frequency of the parameters ε_o and ε_e, as will be shown in the following section for the case of common nematic materials. Therefore, the frequency dispersion equations of $\varepsilon_o(\omega)$ and $\varepsilon_e(\omega)$ can be expressed as

$$\varepsilon_{o/e}(\omega) = \varepsilon_{\infty,o/e} + \frac{(\varepsilon_{s,o/e} - \varepsilon_{\infty,o/e})\Omega_{L,o/e}^2}{\Omega_{L,o/e}^2 + j\omega\Gamma_{L,o/e} - \omega^2}. \quad (29)$$

It can be remarked in Eqs. (24)–(27) that the auxiliary variables obey the differential equation of a Lorentz medium involving the dispersion relation of either $\varepsilon_o(\omega)$ or $\varepsilon_e(\omega)$, and multiplied with nondispersive sine/cosine coefficients. The differential equation of P_{x1} is discretized using central finite differences of second-order accuracy:

$$\left(\frac{\delta_t^2}{\Delta t^2} + \Gamma_{L,o}\frac{\mu_t\delta_t}{\Delta t} + \Omega_{L,o}^2\mu_t^2\right)P_{x1}^n = \varepsilon_0\sin^2\phi\left(\frac{\varepsilon_{\infty,o}}{\Delta t^2}\delta_t^2 + \varepsilon_{\infty,o}\Gamma_{L,o}\frac{\mu_t\delta_t}{\Delta t} + \varepsilon_{s,o}\Omega_{L,o}^2\mu_t^2\right)E_x^n, \quad (30)$$

leading to the following update equation for the variable P_{x1}:

$$P_{x1}^{n+1} = \frac{1}{c_{o1}}(c_{o4}\sin^2\phi E_x^{n+1} + c_{o5}\sin^2\phi E_x^n + c_{o6}\sin^2\phi E_x^{n-1} - c_{o2}P_{x1}^n - c_{o3}P_{x1}^{n-1}), \quad (31)$$

where the coefficients c_{oi}, $i = 1, \ldots, 6$ are given by

$$\begin{aligned}
c_{o1} &= \frac{\Omega_{L,o}}{4} + \frac{\Gamma_{L,o}}{2\Delta t} + \frac{1}{\Delta t^2},\\
c_{o2} &= \frac{\Omega_{L,o}}{2} - \frac{2}{\Delta t^2},\\
c_{o3} &= \frac{\Omega_{L,o}}{4} - \frac{\Gamma_{L,o}}{2\Delta t} + \frac{1}{\Delta t^2},\\
c_{o4} &= \varepsilon_0\left(\frac{\varepsilon_{s,o}\Omega_{L,o}}{4} + \frac{\varepsilon_{\infty,o}\Gamma_{L,o}}{2\Delta t} + \frac{\varepsilon_{\infty,o}}{\Delta t^2}\right),\\
c_{o5} &= \varepsilon_0\left(\frac{\varepsilon_{s,o}\Omega_{L,o}}{2} - \frac{2\varepsilon_{\infty,o}}{\Delta t^2}\right),\\
c_{o6} &= \varepsilon_0\left(\frac{\varepsilon_{s,o}\Omega_{L,o}}{4} - \frac{\varepsilon_{\infty,o}\Gamma_{L,o}}{2\Delta t} + \frac{\varepsilon_{\infty,o}}{\Delta t^2}\right).
\end{aligned} \quad (32)$$

Similar equations can be obtained for the other auxiliary variables, and after substituting the update equations of $P_{x1}, P_{x2}, P_{y1}, P_{y2}$ into Eq. (28), we get the following difference equation for D_x^{n+1}:

$$\begin{aligned}
D_x^{n+1} = {} & a_{x1}E_x^{n+1} + a_{x2}E_x^n + a_{x3}E_x^{n-1} + a_{x4}P_{x1}^n\\
& + a_{x5}P_{x2}^n + a_{x6}P_{x1}^{n-1} + a_{x7}P_{x2}^{n-1}\\
& + a_{y1}E_y^{n+1} + a_{y2}E_y^n + a_{y3}E_y^{n-1} + a_{y4}P_{y1}^n\\
& + a_{y5}P_{y2}^n + a_{y6}P_{y1}^{n-1} + a_{y7}P_{y2}^{n-1}.
\end{aligned} \quad (33)$$

The coefficients a_{xi} are given by

$$\begin{aligned}
a_{x1} &= \frac{c_{o,4}\sin^2\phi}{c_{o,1}} + \frac{c_{e,4}\cos^2\phi}{c_{e,1}},\\
a_{x2} &= \frac{c_{o,5}\sin^2\phi}{c_{o,1}} + \frac{c_{e,5}\cos^2\phi}{c_{e,1}},\\
a_{x3} &= \frac{c_{o,6}\sin^2\phi}{c_{o,1}} + \frac{c_{e,6}\cos^2\phi}{c_{e,1}},\\
a_{x4} &= -\frac{c_{o,2}}{c_{o,1}}, \qquad a_{x5} = -\frac{c_{e,2}}{c_{e,1}},\\
a_{x6} &= -\frac{c_{o,3}}{c_{o,1}}, \qquad a_{x7} = -\frac{c_{e,3}}{c_{e,1}}.
\end{aligned} \quad (34)$$

Similar expressions for the coefficients a_{yi} can be deduced. The difference equation for D_y^{n+1} can be obtained accordingly:

$$\begin{aligned}
D_y^{n+1} = {} & b_{x1}E_x^{n+1} + b_{x2}E_x^n + b_{x3}E_x^{n-1} + b_{x4}Q_{x1}^n + b_{x5}Q_{x2}^n\\
& + b_{x6}Q_{x1}^{n-1} + b_{x7}Q_{x2}^{n-1} + b_{y1}E_y^{n+1} + b_{y2}E_y^n + b_{y3}E_y^{n-1}\\
& + b_{y4}Q_{y1}^n + b_{y5}Q_{y2}^n + b_{y6}Q_{y1}^{n-1} + b_{y7}Q_{y2}^{n-1}.
\end{aligned} \quad (35)$$

The update expressions of E_x^{n+1} and E_y^{n+1} are obtained after solving the 2×2 system of linear equations of (33) and (35). The FDTD update equations of E_x^{n+1} and E_y^{n+1} read

$$E_x^{n+1} = \frac{Ab_{y1} - Ba_{y1}}{a_{x1}b_{y1} - a_{y1}b_{x1}}, \quad (36)$$

$$E_y^{n+1} = \frac{Ba_{x1} - Ab_{x1}}{a_{x1}b_{y1} - a_{y1}b_{x1}}, \quad (37)$$

with

$$A = D_x^{n+1} - a_{x2}E_x^n - a_{x3}E_x^{n-1} - a_{x4}P_{x1}^n - a_{x5}P_{x2}^{n-1} - a_{x6}P_{x1}^{n-1} + a_{x7}P_{x2}^{n-1} + a_{y2}E_y^n - a_{y3}E_y^{n-1} - a_{y4}P_{y1}^n - a_{y5}P_{y2}^n - a_{y6}P_{y1}^{n-1} - a_{y7}P_{y2}^{n-1} \quad (38)$$

and

$$B = D_y^{n+1} - b_{x2}E_x^n - b_{x3}E_x^{n-1} - b_{x4}Q_{x1}^n - b_{x5}Q_{x2}^n - b_{x6}Q_{x1}^{n-1} - b_{x7}Q_{x2}^{n-1} - b_{y2}E_y^n - b_{y3}E_y^{n-1} - b_{y4}Q_{y1}^n - b_{y5}Q_{y2}^n - b_{y6}Q_{y1}^{n-1} - b_{y7}Q_{y2}^{n-1}. \quad (39)$$

It is stressed that proper averaging expressions should be applied on the expressions of A and B for the calculation of each electric component, similarly to the nondispersive anisotropic case. This is necessary in order to avoid instability problems that may arise in simulations due to improper averaging [41]. Also, care should be taken during implementation with respect to the calculation of A and B, and the order by which these are updated.

3. RESULTS

In this section, the accuracy of the proposed FDTD scheme is validated via a series of indicative test examples of photonic structures involving LC materials and/or metallic nanostructures in the visible and near-infrared wavelength ranges. The LC material of choice is the nematic mixture E7, a widely utilized, commercially available material, whose properties have been characterized in detail. As in the case of most organic materials, the material dispersion of the LC ordinary (n_o) and extraordinary (n_e) indices is usually described via a two- or three-coefficient Cauchy model given by

$$n_{o/e}(\lambda) = A_{o/e} + \frac{B_{o/e}}{\lambda^2} + \frac{C_{o/e}}{\lambda^4}, \quad (40)$$

where λ is expressed in micrometers. The Cauchy coefficients for E7 in the 400–1000 nm wavelength window and at a temperature $T = 25°C$ have been calculated equal to $A_e = 1.6933$, $B_e = 0.0078\ \mu m^2$, $C_e = 0.0028\ \mu m^4$ and $A_o = 1.499$, $B_o = 0.0072\ \mu m^2$, $C_o = 0.0003\ \mu m^4$, based on experimentally measured sample values [30]. The expression of the LC relative permittivities $\varepsilon_{r,o/e}(\omega) = n_{o/e}(\omega)^2$ involves complicated rational terms that cannot be readily introduced into a dispersive FDTD algorithm. To this end, the LC material dispersion can be expressed via the Sellmeier model,

$$\varepsilon_{r,o/e}(\lambda) = C_{o/e} + \frac{D_{o/e}\lambda^2}{\lambda^2 - E_{o/e}}, \quad (41)$$

which is equivalent to a lossless Lorentz dispersive model, and it can be directly implemented in the FDTD scheme, as described in Section 2. Figure 2 shows that by employing a simple least-square fitting method, the LC index dispersion of E7 can be described by a single-term Sellmeier model with $C_o = 1.539$, $D_o = 0.707$, $E_o = 0.0316\ \mu m^2$ and $C_e = 2.232$, $D_e = 0.6152$, $E_e = 0.0785\ \mu m^2$. The absolute value of $n_{Sell} - n_{Cau}$ stays below 0.003 for n_e and one order of magnitude lower for n_o. It is stressed that in all examples

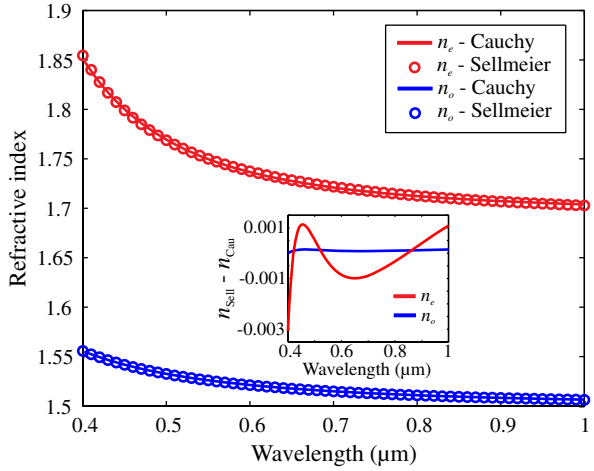

Fig. 2. Sellmeier fitting of the refractive index dispersion for the nematic material E7 in the 400–1000 nm window. The inset shows the difference $n_{Sell} - n_{Cau}$, with reference to the Cauchy model of [30].

investigated in this work, the Cauchy model of Eq. (40) provides the reference LC indices for the purpose of validating the proposed FDTD method. In principle, arbitrary sets of experimentally measured LC index values can be directly fitted to the Sellmeier model and fed into the FDTD algorithm. In addition, although in this study the LC material is considered lossless, the proposed scheme can also incorporate material losses via the damping coefficient Γ in the Lorentz dispersive model.

As a first test example, light transmission through a LC slab placed between cross polarizers is investigated, with a uniform molecular orientation described by the twist angle ϕ as schematically shown in the inset of Fig. 3(b). For the case of incident x-polarized light, i.e., along the axis of the input polarizer, the normalized power transmission after crossing the second polarizer at the exit of the slab is given in a closed form by [42]

$$I_{out} = \sin^2(2\phi)\sin^2\left[\frac{\pi d\Delta n(\lambda)}{\lambda}\right], \quad (42)$$

where $\Delta n(\lambda) = n_e(\lambda) - n_o(\lambda)$ is the wavelength-dependent LC optical anisotropy, d the thickness of the slab, and λ is the operation wavelength. Figure 3(a) shows transmission through a 15 μm thick E7 slab for $\phi = \pi/4$ in the 400–1000 nm window, calculated via the proposed FDTD scheme, employing a spatial step $\Delta z = 2$ nm, and the reference analytic solution, for two cases in which (a) E7 dispersion is included, according to the fitted Sellmeier model of Eq. (41), and (b) E7 is characterized by fixed values $n_o = 1.5222$ and $n_e = 1.739$, which correspond to the LC indices of E7 at 532 nm [30]. This particular set of indices will be used in the rest of this study for the nondispersive-LC reference results. It is demonstrated that the FDTD scheme accurately reproduces the theoretical solution, as evidenced in Fig. 3(b), where the absolute error of the FDTD is plotted for both cases. The dispersive case shows a slightly larger error than the nondispersive one in the low-wavelength spectrum. This is attributed to higher FDTD numerical dispersion, since the corresponding LC indices are higher, particularly n_e as shown

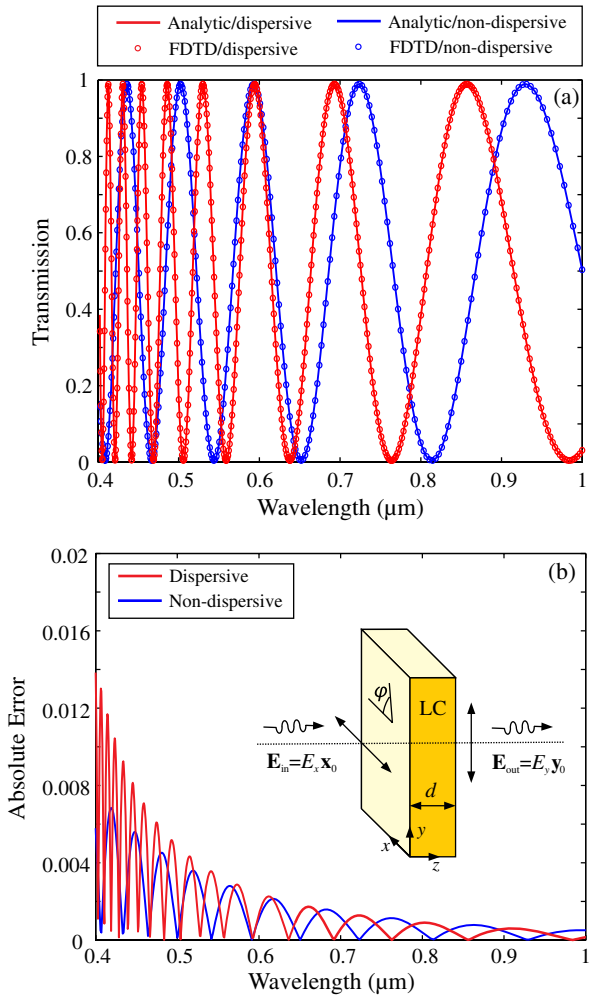

Fig. 3. (a) Transmission of a LC slab placed between cross polarizers calculated by the proposed FDTD method, with and without taking into account the dispersion of the LC indices. Results are compared with the analytic solution. (b) Absolute errors for the two cases examined. Inset shows the schematic layout of the structure.

in Fig. 2, which in turn leads to shorter wavelengths inside the dielectric medium.

Next, we study light transmission through a CLC thin film [43,44] placed between two glass slides of refractive index $n_g = 1.5$, where the nematic host material is E7. The thickness of the slab is equal to $d = 10P_0$, where $P_0 = 450$ nm is the cholesteric helical pitch. The LC permittivity tensor is given by Eq. (20), where the spatial variation of the twist angle is given by $\varphi(z) = 2\pi z/P_0$. The reference solution is calculated by employing the 4×4 Berreman matrix method [37]. Figure 4 shows that the proposed dispersive FDTD implementation satisfactorily reproduces the reference solution. The nondispersive case is also included for comparison, which is shown to deviate from the dispersive reference solution. For instance, the central wavelength and spectral width of the cholesteric bandgap depend on the LC optical birefringence and LC index values. Thus, using a set of LC indices known at a single wavelength, instead of taking into account their dispersion, fails to accurately calculate the overall spectral response of the CLC film.

The examples investigated thus far included only dielectric materials and served to demonstrate the efficiency of the

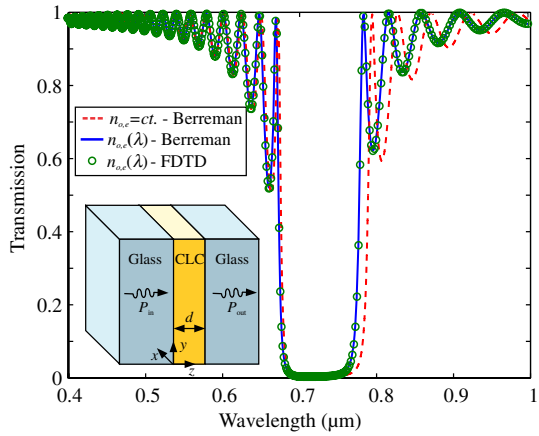

Fig. 4. Transmission through a CLC slab for circularly polarized incident light of the same handedness as the LC helix. Results are compared with those calculated with the 4×4 Berreman matrix method [37]. The proposed FDTD method (circles) accurately reproduces the results obtained for the LC dispersive case (solid line). The nondispersive case (dashed line) is included for comparison. Inset shows the layout of the structure.

proposed anisotropic/dispersive FDTD algorithm for the study of LC-photonic dielectric structures. Combined with the generalized CP model presented in Section 2.A, the proposed scheme can also account for the material dispersion of noble metals, essential elements of plasmonic structures, such as the one shown in Fig. 5. A periodic array of gold nanostripes is placed on a silica substrate of index $n = 1.45$. The nanostripe cross section is $w\times t$, and the array period is $d = 100$ nm. The nematic material E7 constitutes the overlayer of the nanostructure, uniformly orientated at a tilt angle θ and confined in the plane along the axis of the stripes. A y-polarized light impinges from the top, and the optical power transmission P_t is recorded in the silica substrate. CPML and periodic boundary conditions are accordingly applied at the unit cell shown in Fig. 5(b). The LC index dispersion is taken into account via the Lorentz model as explained.

Figure 6 shows the transmission coefficient of the nanostructure for various nanostripe cross sections, for a LC tilt angle $\theta = 0°$. The FDTD results are compared with an investigation based on the frequency-domain FEM [38]. Excellent agreement is observed in the whole spectral region, with maximum relative error in all cases and wavelengths below 1%, for FDTD runs with a $\Delta x = \Delta z = 2$ nm mesh. Figure 7 shows the structure's transmissive properties for $w\times t = 80\times 20$ nm^2 and $d = 100$ nm, when the LC tilt angle ranges from 0° to 45° and 90°, demonstrating that the proposed FDTD scheme can resolve even moderate variations stemming from different LC orientation profiles, by taking rigorously into

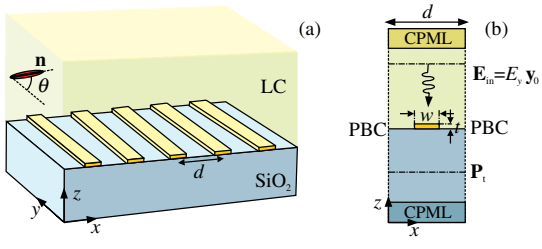

Fig. 5. (a) Schematic layout of the investigated LC-plasmonic structure and (b) FDTD computational domain (unit cell geometry).

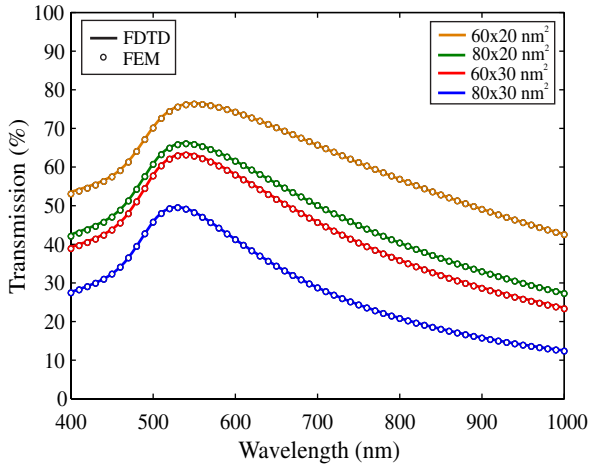

Fig. 6. Transmission coefficient of the nanostripe array of Fig. 5 for $\theta = 0°$ and for various sets of geometrical parameters $w \times t$ of the nanostripes. The proposed FDTD method accurately reproduces results obtained by the FEM.

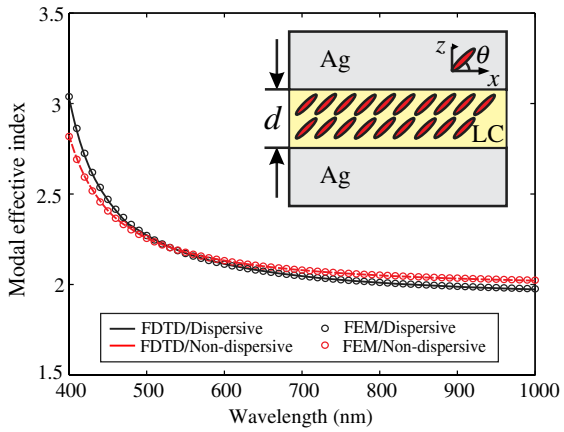

Fig. 8. Effective modal index of a 100 nm thick Ag-E7-Ag plasmonic waveguide for LC tilt angle $\theta = \pi/4$, where the impact of LC material dispersion is also investigated. Results of the proposed FDTD scheme are compared with reference FEM solutions. Inset shows the layout of the MLCM waveguide.

account the material dispersion of both metals and LC materials.

As a last example, we consider the MLCM plasmonic waveguide shown in the inset of Fig. 8. A LC layer with uniform molecular orientation characterized by the tilt angle θ is sandwiched between two silver plates with a separation $d = 100$ nm. Silver is considered as a DCP medium with the parameters of [24]. As in the case of its isotropic metal–insulator–metal counterparts [45], the MLCM plasmonic waveguide supports a fundamental odd TM-polarized mode, whose dispersive properties depend on the LC indices and its orientation [46]. Figure 8 shows the modal effective index in the wavelength window of interest, calculated via the proposed FDTD method and compared with a reference FEM solution for both the dispersive and the nondispersive cases of the LC. The dispersion curve was calculated in a single broadband run. First, two observation points are selected along the direction of propagation, where the electric field is recorded during simulation. Subsequently, the discrete Fourier transform (DFT) of the two time histories was calculated and the propagation constant k_x has been computed via the phase of the ratio of the DFT signals divided by the distance between the two points. At the Ag/LC interface, a simple averaging technique was used, by considering an isotropic effective medium at the FDTD-mesh nodes where the x component of the electric field is defined. The effective medium permittivity is taken equal to $\varepsilon_{\text{eff}}(\omega) = 0.5(\varepsilon_{\text{Ag}}(\omega) + \varepsilon_{xx}(\omega))$, where $\varepsilon_{xx}(\omega)$ is the corresponding element of the LC permittivity tensor. Although this is a heuristic algorithm for the Ag/LC interface treatment, very good results are produced for the LC-anisotropic problem under study, similar to those obtained in [26] for isotropic dielectrics.

The FDTD results of Fig. 8 were obtained using a mesh defined by $\Delta x = 10$ nm and $\Delta z = 5$ nm, and showed a maximum relative error below 0.3% at the low-wavelength edge of the investigated spectral window with respect to the reference FEM solution, when the proposed averaging technique is used at the Ag/LC interface. The effect of LC dispersion can be clearly observed, as the modal dispersion curve notable depends on the values of the LC indices. The two curves cross at 532 nm, which is the wavelength where the set of LC index values was selected for the nondispersive reference case. Neglecting the LC material dispersion leads to an absolute

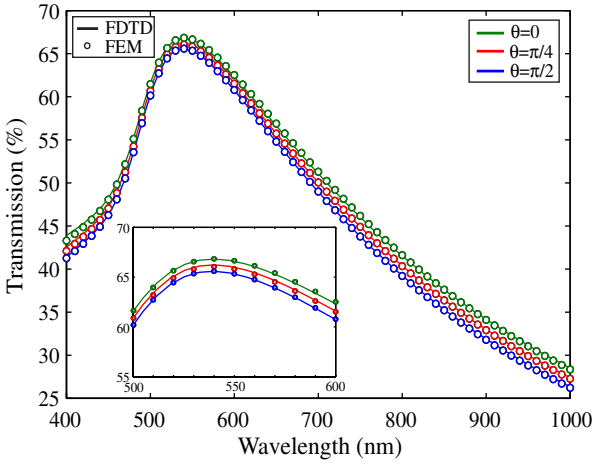

Fig. 7. Transmission coefficient of the nanostripe array of Fig. 5 for $w \times t = 80 \times 20$ nm^2 and for three values of the LC tilt angle θ, calculated by the proposed FDTD and the reference FEM.

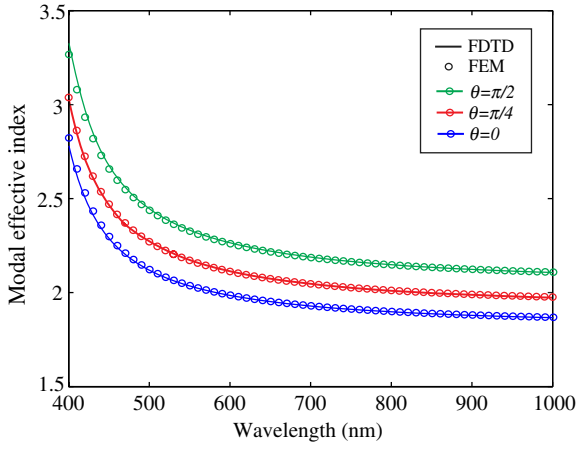

Fig. 9. Effective modal index of the MLCM waveguide studied in Fig. 8 for the dispersive-LC case and for three tilt angle values, $\theta = 0$, $\pi/4$, and $\pi/2$.

relative error of 7.24% and 2.43% at the low- and high-wavelength edges of the spectral window, respectively, indicating the advantage of employing the proposed dispersive FDTD scheme. Finally, Fig. 9 shows the modal dispersion curves for three tilt angle values, $\theta = 0$, $\pi/4$, and $\pi/2$, calculated for the dispersive-LC case, verifying the suitability of the proposed method in the rigorous time-domain study of LC-plasmonic structures. It is stressed that although in these results a uniform LC orientation is assumed, the proposed scheme can readily incorporate complex LC molecular orientation profiles described by spatially varying tilt and twist angles, as in the case of the cholesteric slab investigated in Fig. 4.

4. CONCLUSIONS

In conclusion, we have presented a FDTD scheme for the rigorous study of photonic structures involving nematic LC materials and metallic nanostructures. The model takes into account the full-tensor anisotropy of the LC as well as the permittivity dispersion of all involved materials. Isotropic materials, such as noble metals in the visible or infrared, are modeled via a generalized CPs model, while the dispersion of the LC indices is described by the Lorentz model. The validity of the proposed scheme is verified via a series of test examples demonstrating excellent agreement with reference analytical or numerical solutions.

ACKNOWLEDGMENTS

This work was supported by the Marie-Curie Intra-European Fellowship ALLOPLASM (FP7-PEOPLE-2010-IEF-273528), within the 7th European Community Framework Programme, the Italian Ministry of Foreign Affairs, Directorate General for the Country Promotion, and by the European Union (European Social Fund) and Greek national funds through the Operational Program "Education and Lifelong Learning" of the National Strategic Reference Framework Research Funding Program THALES "Reinforcement of the interdisciplinary and/or inter-institutional research and innovation" (Project ANEMOS).

REFERENCES

1. P. G. De Gennes and J. Prost, *The Physics of Liquid Crystals*, 2nd ed. (Clarendon, 1993).
2. J. Beeckman, K. Neyts, and P. J. M. Vanbrabant, "Liquid-crystal photonic applications," Opt. Eng. **50**, 081202 (2011).
3. D. C. Zografopoulos, R. Asquini, E. E. Kriezis, A. d'Alessandro, and R. Beccherelli, "Guided-wave liquid-crystal photonics," Lab Chip **12**, 3598–3610 (2012).
4. I. Abdulhalim, "Liquid crystal active nanophotonics and plasmonics: from science to devices," J. Nanophoton. **6**, 061001 (2012).
5. P. A. Kossyrev, A. Yin, S. G. Cloutier, D. A. Cardimon, D. Huang, P. M. Alsing, and J. M. Xu, "Electric field tuning of plasmonic response of nanodot array in liquid crystal matrix," Nano Lett. **5**, 1978–1981 (2005).
6. Y. J. Liu, G. Y. Si, E. S. P. Leong, N. Xiang, A. J. Danner, and J. H. Teng, "Light-driven plasmonic color filters by overlaying photoresponsive liquid crystals on gold annular aperture arrays," Adv. Mater. **24**, OP131–OP135 (2012).
7. Q. Hao, Y. Zhao, B. K. Juluri, B. Kiraly, J. Liou, I. C. Khoo, and T. J. Huang, "Frequency-addressed tunable transmission in optically thin metallic nanohole arrays with dual-frequency liquid crystals," J. Appl. Phys. **109**, 084340 (2011).
8. Y. Zhao, Q. Hao, Y. Ma, M. Lu, B. Zhang, M. Lapsley, I.-C. Khoo, and T. J. Huang, "Light-driven tunable dual-band plasmonic absorber using liquid-crystal-coated asymmetric nanodisk array," Appl. Phys. Lett. **100**, 053119 (2012).
9. L. De Sio, A. Cunningham, V. Verrina, C. M. Tone, R. Caputo, T. Bürgi, and C. Umeton, "Double active control of the plasmonic resonance of a gold nanoparticle array," Nanoscale **4**, 7619–7623 (2012).
10. Y. J. Liu, Q. Hao, J. S. T. Smalley, J. Liou, I. C. Khoo, and T. J. Huang, "A frequency-addressed plasmonic switch based on dual-frequency liquid crystals," Appl. Phys. Lett. **97**, 091101 (2010).
11. A. E. Çetin, A. A. Yanik, A. Mertiri, S. Erramilli, Ö. E. Müstecaploğlu, and H. Altug, "Field-effect active plasmonics for ultracompact electro-optic switching," Appl. Phys. Lett. **101**, 121113 (2012).
12. A. C. Tasolamprou, D. C. Zografopoulos, and E. E. Kriezis, "Liquid crystal-based dielectric loaded surface plasmon polariton optical switches," J. Appl. Phys. **110**, 093102 (2011).
13. D. C. Zografopoulos and R. Beccherelli, "Plasmonic variable optical attenuator based on liquid-crystal tunable stripe waveguides," Plasmonics **8**, 599–604 (2013).
14. D. C. Zografopoulos, R. Beccherelli, A. C. Tasolamprou, and E. E. Kriezis, "Liquid-crystal tunable waveguides for integrated plasmonic components," Photon. Nanostr. Fundam. Appl. **11**, 73–84 (2013).
15. D. C. Zografopoulos and R. Beccherelli, "Design of a vertically-coupled liquid-crystal long-range plasmonic optical switch," Appl. Phys. Lett. **102**, 101103 (2013).
16. D. C. Zografopoulos and R. Beccherelli, "Long-range plasmonic directional coupler switches controlled by nematic liquid crystals," Opt. Express **21**, 8240–8250 (2013).
17. J. Beeckman, R. James, F. A. Fernández, W. De Cort, P. J. M. Vanbrabant, and K. Neyts, "Calculation of fully anisotropic liquid crystal waveguide modes," J. Lightwave Technol. **27**, 3812–3819 (2009).
18. E. E. Kriezis and S. J. Elston, "Wide angle beam propagation method for liquid crystal device calculations," Appl. Opt. **39**, 5707–5714 (2000).
19. G. D. Ziogos and E. E. Kriezis, "Modeling light propagation in liquid crystal devices with a 3-D full-vector finite-element beam propagation method," Opt. Quantum Electron. **40**, 733–748 (2008).
20. A. Taflove and S. C. Hagness, *Computational Electrodynamics: The Finite-Difference Time-Domain Method*, 3rd ed. (Artech House, 2005).
21. F. Teixeira, "Time-domain finite-difference and finite-element methods for maxwell equations in complex media," IEEE Trans. Antennas Propag. **56**, 2150–2166 (2008).
22. P. G. Etchegoin, E. C. Le Ru, and M. Meyer, "An analytic model for the optical properties of gold," J. Chem. Phys. **125**, 164705 (2006).
23. A. Vial, "Implementation of the critical points model in the recursive convolution method for modelling dispersive media with the finite-difference time domain method," J. Opt. A **9**, 745–748 (2007).
24. A. Vial, T. Laroche, M. Dridi, and L. Le Cunff, "A new model of dispersion for metals leading to a more accurate modeling of plasmonic structures using the FDTD method," Appl. Phys. A **103**, 849–853 (2011).
25. K. P. Prokopidis and D. C. Zografopoulos, "Efficient FDTD algorithms for dispersive Drude-critical points media based on the bilinear z-transform," Electron. Lett. **49**, 534–536 (2013).
26. K. P. Prokopidis and D. C. Zografopoulos, "A unified FDTD/PML scheme based on critical points for accurate studies of plasmonic structures," J. Lightwave Technol. **31**, 2467–2476 (2013).
27. E. E. Kriezis and S. J. Elston, "Finite-difference time-domain method for light wave propagation within liquid crystal devices," Opt. Commun. **165**, 99–105 (1999).
28. E. E. Kriezis and S. J. Elston, "Light wave propagation in liquid crystal displays by the 2-D finite-difference time-domain method," Opt. Commun. **177**, 69–77 (2000).
29. M. Dridi and A. Vial, "Modeling of metallic nanostructures embedded in liquid crystals: application to the tuning of their plasmon resonance," Opt. Lett. **34**, 2652–2654 (2009).

30. J. Li, C.-H. Wen, S. Gauza, R. Lu, and S.-T. Wu, "Refractive indices of liquid crystals for display applications," J. Display Technol. **1**, 51–61 (2005).
31. L. Yang, "3D FDTD implementation for scattering of electric anisotropic dispersive medium using recursive convolution method," Int. J. Infrared Millim. Waves **28**, 557–565 (2007).
32. H. Mosallaei, "FDTD-PLRC technique for modeling of anisotropic-dispersive media and metamaterial devices," IEEE Trans. Electromagn. Compat. **49**, 649–660 (2007).
33. S. Huang and F. Li, "FDTD simulation of electromagnetic propagation in magnetized plasma using Z transforms," Int. J. Infrared Millim. Waves **25**, 815–825 (2004).
34. V. Nayyeri, M. Soleimani, J. Rashed-Mohassel, and M. Dehmollaian, "FDTD modeling of dispersive bianisotropic media using Z-transform method," IEEE Trans. Antennas Propag. **59**, 2268–2279 (2011).
35. A. A. Al-Jabr, M. A. Alsunaidi, T. Khee, and B. S. Ooi, "A simple FDTD algorithm for simulating EM-wave propagation in general dispersive anisotropic material," IEEE Trans. Antennas Propag. **61**, 1321–1326 (2013).
36. J. A. Roden and S. D. Gedney, "Convolution PML (CPML): an efficient FDTD implementation of the CFS-PML for arbitrary media," Microw. Opt. Technol. Lett. **27**, 334–339 (2000).
37. S. Stallinga, "Berreman 4×4 matrix method for reflective liquid crystal displays," J. Appl. Phys. **85**, 3023–3031 (1999).
38. COMSOL Multiphysics v4.3a.
39. A. Vial and T. Laroche, "Description of dispersion of metals by means of the critical points model and application to the study of resonant structures using the FDTD method," J. Phys. D **40**, 7152–7158 (2007).
40. J. Pereda, L. Vielva, A. Vegas, and A. Prieto, "Analyzing the stability of the FDTD technique by combining the von Neumann method with the Routh-Hurwitz criterion," IEEE Trans. Microwave Theor. Tech. **49**, 377–381 (2001).
41. G. R. Werner and J. R. Cary, "A stable FDTD algorithm for non-diagonal, anisotropic dielectrics," J. Comput. Phys. **226**, 1085–1101 (2007).
42. I.-C. Khoo, *Liquid Crystals*, 2nd ed. (Wiley, 2007).
43. D. C. Zografopoulos, E. E. Kriezis, M. Mitov, and C. Binet, "Theoretical and experimental optical studies of cholesteric liquid crystal films with thermally induced pitch gradients," Phys. Rev. B **73**, 061701 (2006).
44. A. C. Tasolamprou, M. Mitov, D. C. Zografopoulos, and E. E. Kriezis, "Theoretical and experimental studies of hyperreflective polymer-network cholesteric liquid crystal structures with helicity inversion," Opt. Commun. **282**, 903–907 (2009).
45. J. A. Dionne, L. A. Sweatlock, H. A. Atwater, and A. Polman, "Plasmon slot waveguides: towards chip-scale propagation with subwavelength-scale localization," Phys. Rev. B **73**, 035407 (2006).
46. D. C. Zografopoulos and R. Beccherelli, "Liquid-crystal tunable metal-insulator-metal plasmonic waveguides and Bragg resonators," J. Opt. **15**, 055009 (2013).